Influence of Gd Doping on the Structure and Electrochemical Behavior of UO₂

Nazhen Liu[a], Jandee Kim[b], Jeongmook Lee[b], Young-Sang Youn[b], Jong-Goo Kim[b], Jong-Yun Kim[b,c,**], James J. Noël[a,d], David W. Shoesmith[a,d,*]

[a] Department of Chemistry, The University of Western Ontario, London, Ontario, N6A 5B7, Canada
[b] Nuclear Chemistry Research Division, Korea Atomic Energy Research Institute, Daejeon, 34057, Republic of Korea
[c] Radiochemistry & Nuclear Nonproliferation, University of Science & Technology, Daejeon, 34113, Republic of Korea
[d] Surface Science Western, The University of Western Ontario, London, Ontario, N6G 0J3, Canada

ABSTRACT

A series of $(U_{1-y}Gd_y)O_2$ materials ($y = 0$, 0.01, 0.03, 0.05, 0.07 and 0.10) were characterized by X-ray diffractometry and Raman spectroscopy to determine the influence of Gd^{III} doping on the structure of $(U_{1-y}Gd_y)O_2$ solid solutions. The XRD results show that, while the fluorite structure is maintained, Gd doping up to 10% leads to a contraction of the fluorite lattice. Raman spectroscopy shows Gd^{III} doping distorts the fluorite lattice structure due to the formation of oxygen vacancies (O_v) and, possibly, MO_8-type complexes, as a consequence of the differences in both the oxidation state and the ionic radius of Gd^3+ compared to that of the U^{4+}. The influence of Gd doping on the electrochemical reactivity of the $(U_{1-y}Gd_y)O_2$ specimens was shown to be minor, possibly due to a competition between the increase in the number of O_v and the contraction of the lattice.

© 2017 Elsevier Ltd. All rights reserved.

1. Introduction

The recommended approach for the long-term management of used nuclear fuel in Canada is adaptive phased management [1,2]. As accepted internationally, the repository concept is based on multiple barriers including the fuel bundles, durable metal containers, a clay buffer and seals around the container, and a deep geologic environment [3]. A key barrier is the corrosion-resistant container that will be designed to isolate the used fuel indefinitely [4,5]. However, it is judicious to examine the consequences of container failure and the exposure of used fuel bundles to groundwater. Since U is considerably more soluble in the oxidized (U^{VI}) than the reduced form (U^{IV}) [6], its dissolution, leading to the release of radionuclides, must proceed via corrosion. In the anoxic conditions anticipated in a deep geological repository, water radiolysis, resulting from the radiation fields associated with the used fuel, will be the only source of oxidants. Of the oxidants formed by radiolysis, H_2O_2 has been shown to be the primary oxidant driving fuel corrosion [7,8].

The reactivity of the UO₂ matrix, and how it is modified by in-reactor irradiation, is important in determining fuel corrosion. The key changes likely to influence the chemical reactivity of the fuel are the rare earth (RE) doping of the matrix, the presence of noble metal particles and the development of non-stoichiometry [9]. Considerable experimental evidence exists to show that fission product and actinide-lanthanide doping have a significant effect on the kinetics of air oxidation of the fuel [10,11]. Choi et al. investigated the oxidation of UO₂ based SIMFUEL (1.5, 3.0, 4.0, 6.0 and 8.0 at%), and showed that oxidation of 6 and 8 at% SIMFUEL yielded a cubic phase, and that the time to convert UO₂ to U_3O_8 increased with simulated burnup at 250 °C [12]. Talip et al. studied the air oxidation of La-doped UO₂ at 500 K and concluded that La doping causes a lattice expansion which increases diffusion of O^{2-} ions in the UO₂ matrix, leading to its prompt oxidation in air, which stops after the formation of an M_4O_9 phase [13]. You et al. showed that the weight gain due to oxidation of 15 wt% Gd_2O_3 doped UO₂ at 350 °C is only half that of the un-doped UO₂ [14]. Kim et al. studied

---

the effect of Gd^{III}, as a dopant in UO_2 on its oxidation using thermogravimetry and XRD analysis. The degree of oxidation from UO_2 to U_3O_8 was found to decrease linearly with increasing Gd content, suggesting the Gd dopant can slow down the initial oxidation kinetics from UO_2 to U_4O_9, and prevent the complete oxidation to U_3O_8 [15]. Razdan and Shoesmith showed that the electrochemical oxidation/dissolution mechanism of Gd-doped UO_2 is similar to that of SIMFUEL, although the overall reactivity is lower. It was proposed that this could be attributed to the presence of Gd^{III}-O_v (O_v: oxygen vacancy) clusters which reduce the availability of the (O_v)s required to accommodate excess O^{II} ions when oxidation occurs [16,17].

Since there has been a continuous trend toward higher in-reactor fuel burnup [18], the extent of doping and its influence on fuel reactivity under waste disposal conditions is becoming more important. In this study, a series of $(U_{1-y}Gd_y)O_2$ materials ($y = 0$, 0.01, 0.03, 0.05, 0.07 and 0.10) were synthesized, characterized by XRD and Raman spectroscopy, and the reactivity of the $(U_{1-y}Gd_y)O_2$ matrix investigated electrochemically. Since the key groundwater constituents likely to influence fuel dissolution are HCO_3^-/CO_3^{2-}, which will increase UO_2^{2+} solubility by complexing UO_2^{2+} [6], these studies were conducted in solutions containing HCO_3^-/CO_3^{2-}.

2. Experimental

2.1. Materials and preparation

$U_{1-y}Gd_yO_2$ pellets with various compositions ($y = 0$, 0.01, 0.03, 0.05, 0.07 and 0.10) were synthesized using a conventional solid-state process involving the mixing of oxide powders. Appropriate amounts of UO_2 and Gd_2O_3 (Aldrich, >99.99%) powder were mixed and thoroughly blended in an agar mortar. The blended powders were then pressed into a disk-shaped pellet and sintered at 1700 °C for 18 h in a reducing atmosphere with flowing hydrogen. The sintered pellets were then cooled to room temperature in flowing hydrogen after annealing in the same atmosphere at 1200 °C for 12 h.

2.2. X-ray diffraction

X-ray diffraction (XRD) patterns were measured with a Bruker AXS D8 Advance X-ray Diffractometer using Cu K_α radiation at room temperature. XRD data were collected from several locations on the sintered pellets to confirm the homogeneity in structure. The lattice parameters of the solid solution samples were determined over the 2θ range from 20° to 120° using a 0.02° step size. The lattice parameters of the samples were calculated by a refinement process using the TOPAS program (Bruker Analytical X-Ray Systems) with the $Fm\bar{3}m$ space group.

2.3. Raman Spectroscopy

The Raman spectroscopic measurements were carried out with an ANDOR Shamrock SR500i spectrometer, with active vibrations excited using a He-Ne laser with a wavelength of 632.8 nm. The laser, with a power of ∼5 mW, was focused onto the pellets using an Olympus microscope with a 50-fold magnification lens. This laser power was confirmed to be low enough to prevent surface oxidation of the pellets, due to local heating effects by the laser beam. Raman spectra were acquired over the wavenumber range from 400 to 1200 cm^{-1} using an exposure time of 300 s. Spectra were collected from different locations on the surface of pellets to confirm their reproducibility and the homogeneity of composition.

2.4. Electrochemical procedures

Experiments were performed in a standard three-electrode cell. A commercial saturated calomel reference electrode (SCE) (+0.242 V, 25 °C vs. standard hydrogen electrode (SHE)) was used,
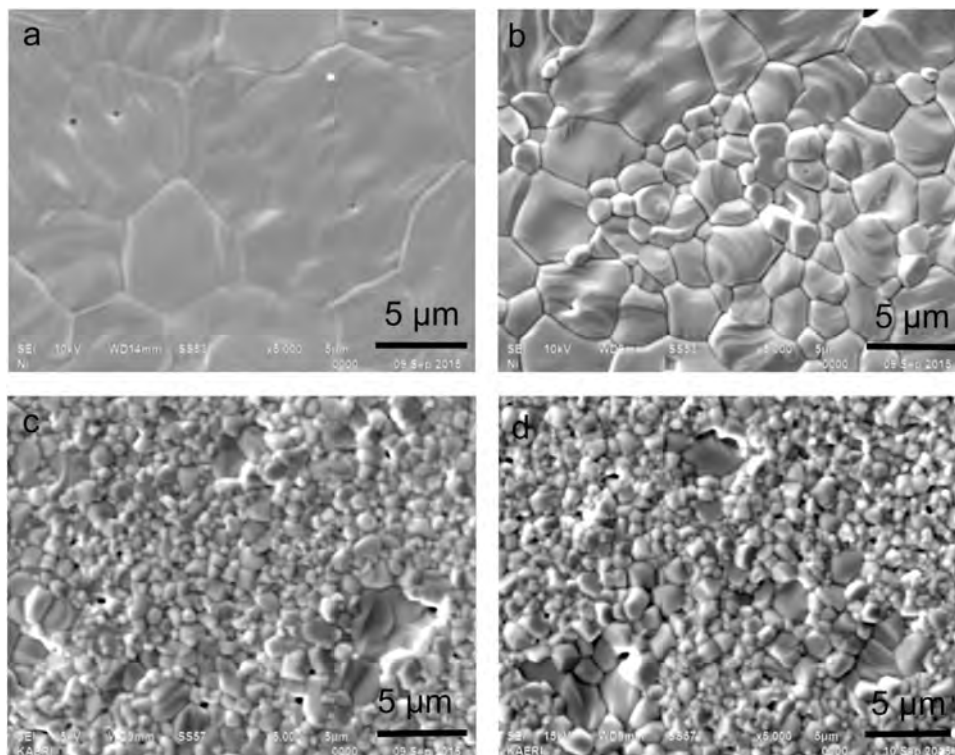

Fig. 1. SEM images recorded on $U_{1-y}Gd_yO_2$ specimens (a, $y = 0$; b, $y = 0.01$; c, $y = 0.03$ and d, $y = 0.07$).

and a Pt wire with a spot-welded Pt foil was employed as the counter electrode. All potentials were quoted on the SCE scale. All electrochemical experiments were carried out using a CHI-600D potentiostat to control applied potentials and record current responses. IR compensation was employed to compensate voltage drops due to ohmic resistance in the electrodes. Prior to experiments, electrodes were prepared by polishing using wet 3000 grit SiC paper and rinsed with distilled deionized water. Subsequently, the electrodes were electrochemically reduced at −1.2 V for 5 min (vs. SCE) to remove any air-formed oxides or organic contaminants present on the surface.

2.5. Solution preparation

Solutions were prepared using distilled deionized water (resistivity $\rho = 18.2\,M\Omega\cdot cm$) purified using a Millipore Milli-Q plus unit which removes organic and inorganic impurities. The base electrolyte was $0.1\,mol\,L^{-1}$ NaCl (Aldrich). The HCO_3^-/CO_3^{2-} concentrations were adjusted with Na_2CO_3 and $NaHCO_3$ (Aldrich). The total carbonate concentration ($[CO_3]_T = [HCO_3^-] + [CO_3^{2-}]$) was $0.05\,mol\,L^{-1}$ with the pH maintained constant at 10 using an Orion model 720A pH meter. Prior to an experiment, the solution in the cell was purged with Ar-gas (Shinhan Gas) for an hour and purging was then maintained throughout the experiment.

3. Results and Discussion

3.1. Surface morphology

Fig. 1 shows that the morphology of the surface for $U_{1-y}Gd_yO_2$ changes as the doping level increases from 0 to 3%, but then remains unchanged up to 7%. Also a number of voids are visible on the surface, introducing the possibility that the reactivity may not be totally uniform.

3.2. XRD Analysis

The XRD patterns (not shown here) show that the specimens retain the fluorite structure with no XRD peaks observed for the monoclinic Gd_2O_3 impurity [19]. Fig. 2 compares the lattice parameter as a function of Gd determined in this study with the values measured by Kim [15], Ohmichi [20] and Baena [21]. The lattice parameter decreases as the Gd doping level increases. The lattice contraction could be caused by one or other (or both) of two charge compensation mechanisms: one involves the creation of U^V (the radius of the U^{5+} ion (r = 0.088 nm) is smaller than that of the U^{4+} ion (0.1001 nm)), and the other the formation of (O_v)s (O_v:

Table 1
The formation of U^V and oxygen vacancies to neutralize the charge introduced by Gd doping.

	$y^a = 0$	$y = 0.01$	$y = 0.05$	$y = 0.10$
m in $(U_{1-y-m}^{IV}U_m^V Gd_y^{III})O_2$ [b]	0	0.01	0.05	0.10
n in $(U_{1-y}^{IV}Gd_y^{III})O_{2-n}$ [c]	0	0.005	0.025	0.05

[a] y as in $U_{1-y}Gd_yO_2$, indicating the Gd doping level.
[b] Assuming the creation of U^V is the only charge neutralization feature introduced by doping.
[c] Assuming the creation of oxygen vacancies is the only charge neutralization feature introduced by doping.

oxygen vacancy) (Table 1). He et al. studied the influence of fission product doping on the structure of SIMFUELs [22]. As the doping level increased, the X-ray photoelectron spectroscopic (XPS) data indicated an increase in U^V content, while deconvolution of the Raman spectra indicated the increasing formation of $RE^{III}-O_v$ clusters, suggesting either both charge compensation mechanisms are operative or they cannot be distinguished in SIMFUELs. Compared with the results of Ohmichi [20] and Baena [21], this work yields a slightly larger lattice parameter (Fig. 2), which could be attributable to a slight hypo-stoichiometry of our specimens [20]. According to the relationship between the degree of hypo-stoichiometry x (in $U_{1-y}Gd_yO_{2-x}$) and the lattice parameter (a) proposed by Ohmichi [20] (Eq. (1)),

$$\frac{da}{dx} = 0.024 \pm 0.006 \text{ nm} \tag{1}$$

the degree of hypo-stoichiometry (x in $U_{1-y}Gd_yO_{2-x}$) in our specimens could be between 0.012 ($y = 0$) and 0.025 ($y = 0.1$).

3.3. Raman spectroscopy

Raman spectroscopy has been commonly used to investigate the structure of the U-O system [13,17,22–26]. UO_2 has a cubic fluorite structure and belongs to the space group O_h ($Fm\overline{3}m$) and should generate a triply degenerate Raman active (T_{2g}) mode at $\sim445\,cm^{-1}$, assigned to the O-U stretch, and a band at $\sim1150\,cm^{-1}$, assigned as an overtone (2L-O) of the first order L-O phonon ($\sim575\,cm^{-1}$). It has been suggested that the band at $\sim1150\,cm^{-1}$ can be taken as a fingerprint for the quasi-perfect fluorite structure, since its intensity decreases considerably as the defect structure develops, due to increasing non-stoichiometry. [25].

Fig. 3 shows the Raman spectra of the $U_{1-y}Gd_yO_2$ specimens ($y = 0, 0.01, 0.05$ and 0.07). While all four exhibit a similar structure, the relative peak intensities differ considerably. For UO_2 (Fig. 3A), the peaks at $450\,cm^{-1}$ and $1150\,cm^{-1}$ are dominant compared to

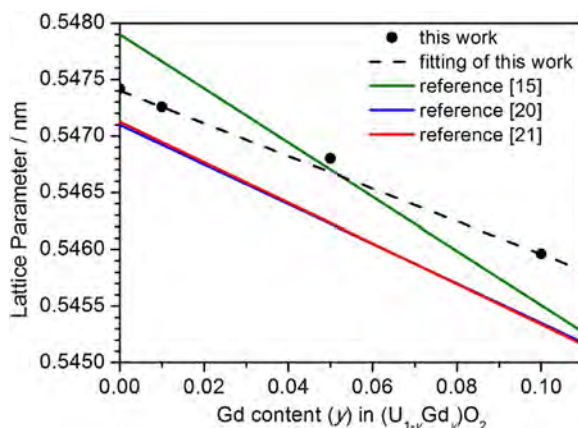**Fig. 2.** Lattice parameters of $U_{1-y}Gd_yO_2$ specimens as a function of Gd content in this work, including comparison with the reference results.
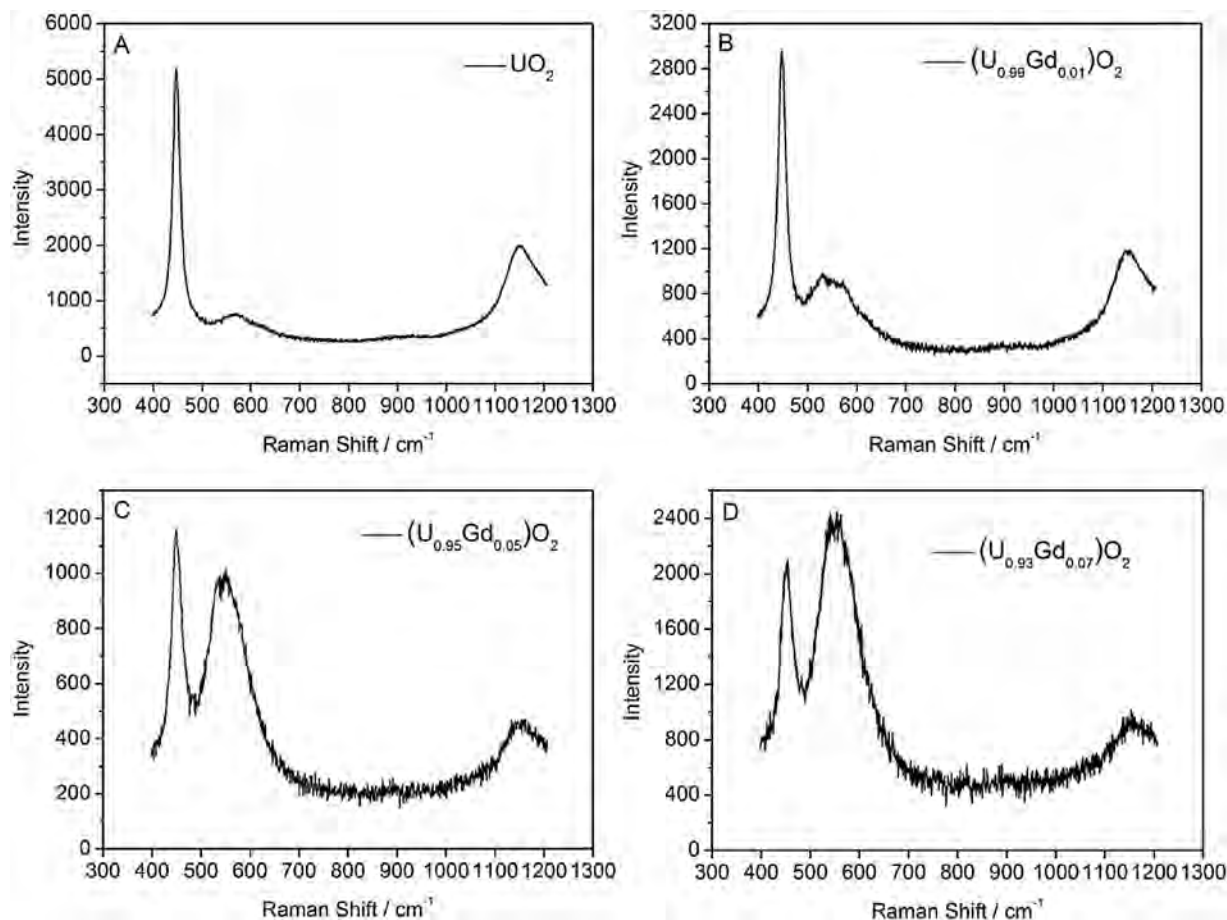
Fig. 3. Raman spectra recorded on $U_{1-y}Gd_yO_2$ specimens (a, $y = 0$; b, $y = 0.01$; c, $y = 0.05$ and d, $y = 0.07$).

the broad band between 500–700 cm^{-1}, indicating the lattice is relatively defect free. As the extent of Gd doping increases, the relative intensity of the two bands at 445 cm^{-1} and 1150 cm^{-1} decrease with respect to the broad band (between 500–700 cm^{-1}), which has been attributed to UO$_2$ lattice damage, due to the formation of the defects caused by doping [22].

Li et al. [27] studied the defect sites for a series of dopants in Ce$_{0.8}$M$_{0.2}$O$_{2-\delta}$ solid solutions (CeO$_2$ has a similar fluorite lattice to UO$_2$) using Raman spectroscopy, and investigated the effects of different valence states and ionic radii of the dopants on the spectral features of these materials. A peak at ∼560 cm^{-1}, observed on Ce$_{0.8}$Pr$_{0.2}$O$_{2-\delta}$ was assigned to the creation of O$_v$, due to the difference in ionic valence states between Pr^{n+} (n = 3∼4) and Ce^{4+}, Pr^{n+} having a similar average ionic radius to Ce^{4+}. A peak at ∼600 cm^{-1}, observed on Ce$_{0.8}$Zr$_{0.2}$O$_{2-\delta}$ was assigned to the formation of a ZrO$_8$-type complex, Zr^{4+} (0.084 nm) and Ce^{4+} (0.097 nm) having very different ionic radii. For Ce$_{0.8}$Gd$_{0.2}$O$_{2-\delta}$, two bands are observed simultaneously at approximately 560 and 600 cm^{-1}, suggesting the presence of both defect structures when both the oxidation state and the ionic radius of the dopant differ from that of the matrix cation. He et al. studied the defect structures of hyper-stoichiometric UO$_{2+x}$ using Raman spectroscopy [23], and demonstrated that a band at 630 cm^{-1} became increasingly more prominent as the O defect content increased. This 630 cm^{-1} band was assigned to the A$_{1g}$ stretch due to the formation of cuboctahedral clusters. This assignment was

confirmed by Desgranges et al. [24]. Talip et al. [13] studied the La doped UO$_2$ and assigned the 630 cm^{-1} band to the formation of U$_4$O$_9$ under oxidation conditions.

The deconvolution of the broad band in our spectra is shown in Fig. 4. The 450 cm^{-1} peak is treated as Lorentzian while those at 540, 575 and 620 cm^{-1} are treated as Gaussian. The peak at 540 cm^{-1} is not observed in UO$_2$ (Fig. 4A) but increases as the doping level increases (Fig. 4B to D), confirming it can be assigned to the creation of Gd^{III}-oxygen vacancy (O$_v$) clusters. The presence of O$_v$ in UO$_2$ is consistent with the calculations of Park [28], and the observations of Desgranges, who attributed a peak at this wavenumber (recorded on Nd-doped UO$_2$) to a local phonon mode associated with O$_v$-induced lattice distortion [29]. The intensity of the peak at 620 cm^{-1} also increases as the doping level increases, suggesting the possible presence of MO$_8$-type complexes as claimed by Li et al. [27] when Gd was the dopant. As noted above the peak at 575 cm^{-1} is due to the first order L-O phonon and is associated with the close to perfect fluorite lattice.

Fig. 5 shows the area ratios of the peaks at 540, 575 and 620 cm^{-1} versus the T$_{2g}$ peak (450 cm^{-1}). The ratio between the 540 cm^{-1} peak and the T$_{2g}$ peak increases as the doping level increases up to 7%, and then decreases. Since the T$_{2g}$ peak is characteristic of the undisturbed fluorite lattice and the 540 cm^{-1} peak is related to the creation of O$_v$ associated with the Gd^{III} doping, this suggests the formation of O$_v$ becomes less important than the charge compensation mechanism when the doping level
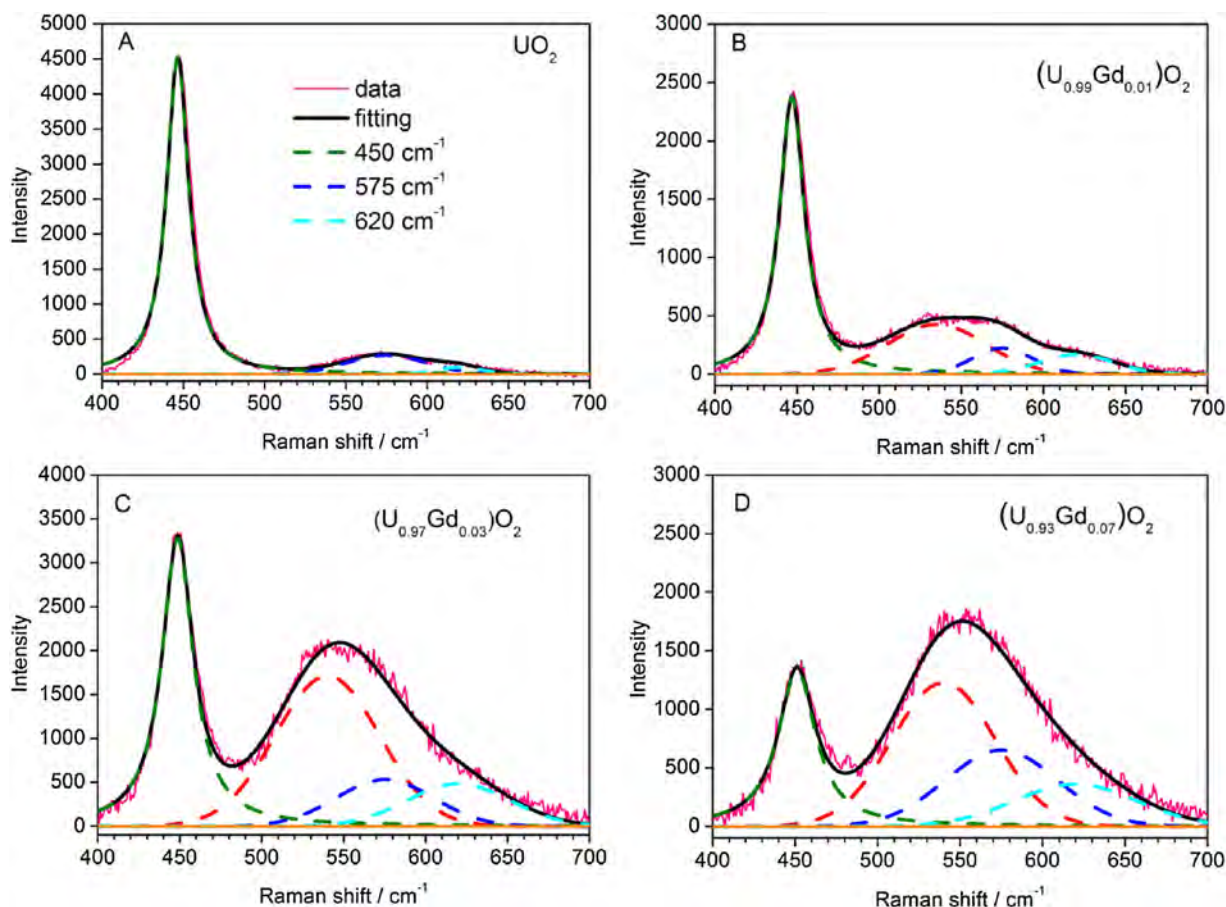
Fig. 4. Deconvoluted Raman spectra of $U_{1-y}Gd_yO_2$ specimens (a, $y = 0$; b, $y = 0.01$; c, $y = 0.03$ and d, $y = 0.07$).
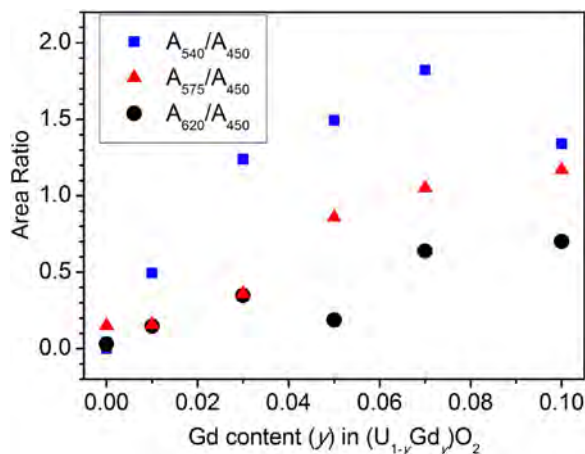

Fig. 5. Area ratios of the Raman peaks recorded at 540 cm^{-1}, 575 cm^{-1} and 620 cm^{-1} versus the T_{2g} peak at 450 cm^{-1} as a function of the Gd doping level.

is high; i.e., 10%. The area ratio between the 620 cm^{-1} peak and the T_{2g} peak increases as the doping level increases, suggesting an increase in importance of MO_8-type complexes as the lattice is disturbed by the Gd^{III} doping. The alternative assignment of a peak in this spectral region to a hyperstoichiometric cuboctahedral cluster can be ruled out in our specimens, which are close to stoichiometric and possibly slightly hypostoichiometric. The peak at 575 cm^{-1} was shown to be independent of doping level in a series of SIMFUELs investigated previously [22]. However, in this study, the area ratio (A_{575}/A_{450}) increases as the doping level

increases, most likely due to a breakdown in selection rules as the presence of defects increases, making the forbidden first order L–O Raman scattering mode (575 cm^{-1}) allowed [23].

Whether or not MO_8-type clusters are present is uncertain since deconvolution of the Raman spectra was found to be very sensitive to the peak shape adopted when fitting the spectra. Fig. 6 compares the deconvoluted Raman spectra for our $U_{0.93}Gd_{0.07}O_2$ specimen obtained using different assumed peak shapes. While the 450 cm^{-1} peak is treated as Lorentzian in both fits, the peaks at 540, 575 and 620 cm^{-1} are assigned as Gaussian peaks in Fig. 6A and Lorentzian
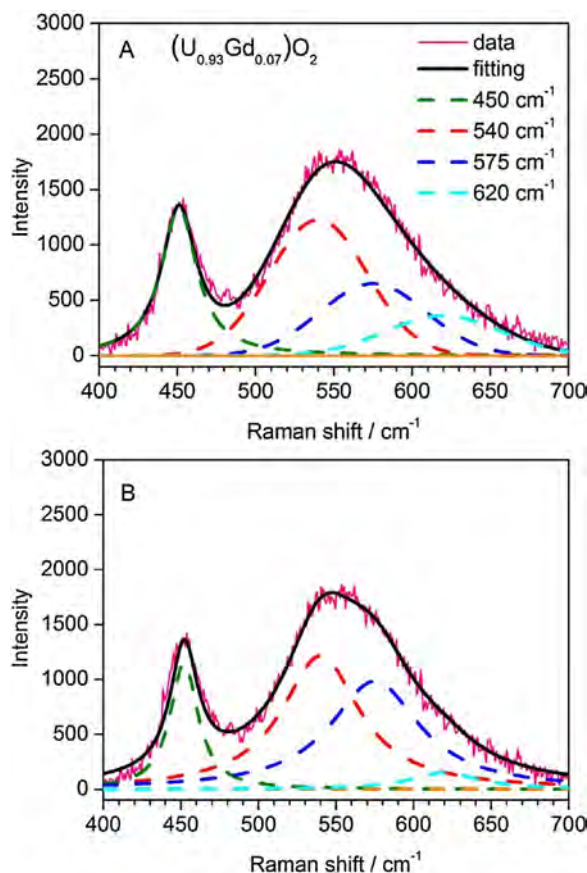
Fig. 6. Deconvoluted Raman spectrum of $U_{0.93}Gd_{0.07}O_2$. The peaks at 540, 575 and 620 cm^{-1} are treated as Gaussian peaks in (A) and Lorentzian peaks in (B).

peaks in Fig. 6B. In the latter case (Fig. 6B) the 620 cm^{-1} peak becomes marginal.

3.4. Electrochemical study

When perfectly stoichiometric, UO_2 is best described as a Mott-Hubbard insulator. The introduction of electronic conductivity requires promotion of electrons from the occupied U 5f level to the conduction band, which is a strongly activated process with a low probability at room temperature. However, replacement of a fraction of the U^{IV} ions with RE^{III} ions requires further ionization of the remaining uranium ions (to U^V) or the creation of oxygen vacancies (O_v) to maintain overall charge balance (Table 1). The former creates mobile holes in the U 5f band, resulting in an increased conductivity [30]. Table 2 summarizes the total cell resistances for the four electrodes investigated, with the resistance being effectively that of the $U_{1-y}Gd_yO_2$ electrode. As expected, the undoped UO_2 has a relatively high resistance compared with the $(U_{0.99}Gd_{0.01})O_2$ electrode. However, increased doping leads to only a marginal further increase in conductivity. A possible explanation for this is that the expected increase in conductivity due to doping

is offset by the lattice disorder introduced by Gd^{III}-O_v clustering. However, Fig. 5 suggests the formation of O_v becomes less important as the doping level increases up to 10%, suggesting the formation of O_v is only part of the reason for the marginal increase in conductivity. A second possible explanation based on impedance measurements [31] would be that, there are two conductivity pathways on the Gd-doped UO_2 specimens, matrix and grain boundary. According to Kubo et al. [31], while matrix conductivity increases linearly with increased doping, the grain boundary conductivity decreases, the latter being attributed to segregation of Gd to the grain boundaries, leading to the formation of a potential barrier against the migration of holes in the U5f level. These conflicting effects could result in the insensitivity of the conductivity to doping [31]. Even though impedance spectroscopy is widely used in testing the conductivity of solid-state materials [31–33], the adoption of an electrical equivalent circuit involving two time constants in series to represent grain and grain boundary conductivities is suspect. Faber et al. [34] proposed that doping could cause the appearance of percolation paths associated with a low activation energy, while the creation of deep traps because of multiple trapping could lead to an increase of the activation

Table 2
Resistance of the circuits (mainly from the electrodes) measured by the potentiostat in 0.1 M NaCl with and without 0.05 M $Na_2CO_3/NaHCO_3$.

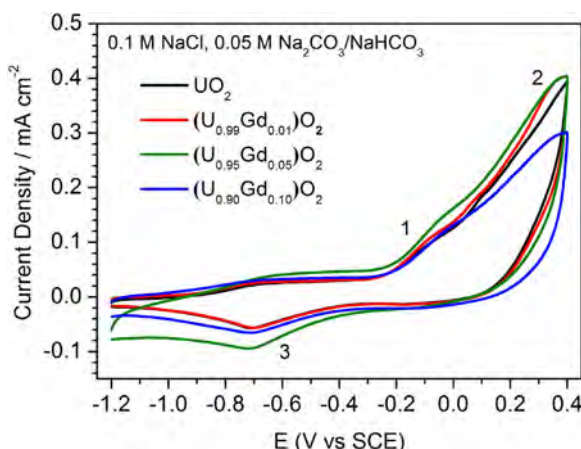| Electrode	Resistance (ohms) in 0.1 M NaCl	Resistance (ohms) in 0.1 M NaCl and 0.05 M $Na_2CO_3/NaHCO_3$
UO_2	261.6	245.1
$(U_{0.99}Gd_{0.01})O_2$	53.1	38.6
$(U_{0.95}Gd_{0.05})O_2$	50.8	37.9
$(U_{0.90}Gd_{0.10})O_2$	51.2	37.4

Fig. 7. CVs recorded on freshly polished $(U_{1-y}Gd_y)O_2$ electrodes in an Ar purged 0.1 M NaCl with 0.05 M Na_2CO_3/$NaHCO_3$ solution, pH = 10. The scan rate = 10 mV s^{-1}.

energy. These compensating effects offer an alternative explanation for the insensitivity of conductivity to the doping level for the Gd-doped UO_2 specimens.

3.4.1. Cyclic Voltammetry

Fig. 7 shows a series of CVs recorded on the undoped and Gd[III]-doped UO_2 electrodes. As observed for SIMFUEL [35] and previously for Gd-doped UO_2 [16], the electrodes exhibit similar stages of oxidation and reduction. On the positive scan, the current in region 1 can be attributed to the oxidation of a thin surface layer to a mixed U^{IV}/U^{V} oxide ($U^{IV}_{1-2x}U^{V}_{2x}O_{2+x}$), with a thickness limited by diffusion of O to subsurface locations. Oxidation at higher potentials (region 2 in Fig. 7) was attributed to the oxidation of this $U^{IV}_{1-2x}U^{V}_{2x}O_{2+x}$ layer to U^{VI}, most of which will dissolve as UO_2^{2+} complexed by HCO_3^-/CO_3^{2-}. On the reverse scan, the extent of surface oxidation (not including the U dissolved) can be gauged by the size of the reduction peak 3. Comparison of the CVs shows that the reactivity in region 1 is insensitive to the doping level and only decreased in region 2 at the highest doping level ($y = 0.1$). Similarly, on the reverse scan, the current associated with the reduction of the surface does not vary significantly with doping level.

3.4.2. Potentiostatic Polarization

Since CVs are performed rapidly, they may not faithfully capture the differences in reactivity levels due to doping. These differences may be more realistically assessed under steady-state conditions. Fig. 8 shows potentiostatic polarization curves recorded on the $U_{0.95}Gd_{0.05}O_2$ electrode for potentials at the positive end of region 1 (0.1 V) and in region 2 (0.2 V to 0.5 V). At the two lowest potentials (0.1 V and 0.2 V), the current decreases linearly (on the logarithmic scale) especially at the lowest potential. This is consistent with a loss in surface reactivity associated with the formation of a $U^{IV}_{1-2x}U^{V}_{2x}O_{2+x}$ thin surface layer. At longer times, the current continues to decrease at 0.1 V but begins to stabilize at a steady-state value at 0.2 V, indicating the onset of region 2; i.e., the conversion of this layer to soluble $U^{VI}O_2^{2+}$. At 0.3 V and higher, a steady state current independent of potential is much more rapidly achieved. As previously shown for 6 wt% Gd-doped UO_2, this potential-independent current can be attributed to the electrochemical formation of a $U^{VI}O_2CO_3$ surface layer (Eq. (2)),

$$U^{IV}_{1-2x}U^{V}_{2x}O_{2+x} + CO_3^{2-} \rightarrow U^{VI}O_2CO_3 \qquad (2)$$
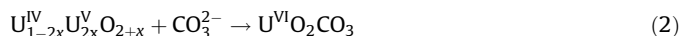
whose subsequent dissolution is chemically-controlled (Eq. (3)).

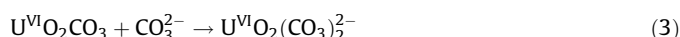$$U^{VI}O_2CO_3 + CO_3^{2-} \rightarrow U^{VI}O_2(CO_3)_2^{2-} \qquad (3)$$

Fig. 9 shows the steady-state currents recorded in region 2 (Fig. 7) as a function of the Gd content of the matrix. At low Gd contents (up to ~$y = 0.03$ to 0.05), the current, which is due to steady-state dissolution (as $U^{VI}O_2(CO_3)_2^{2-}$) is either independent of
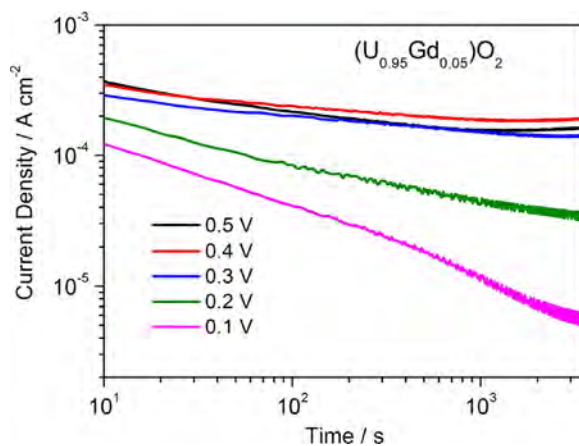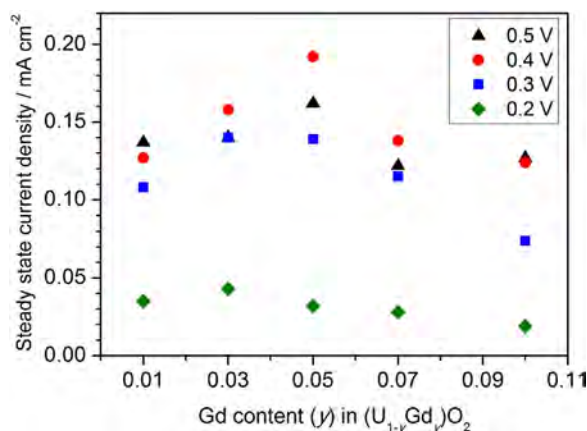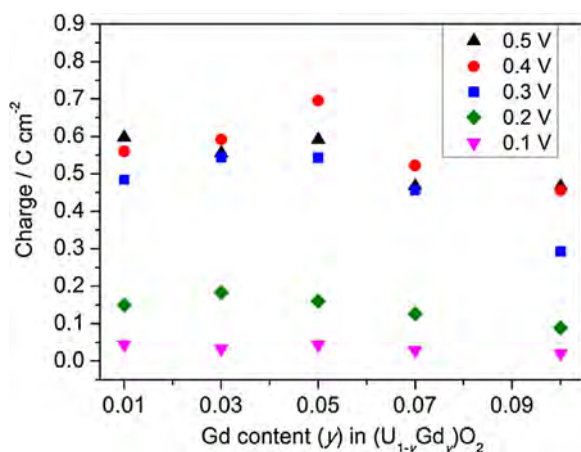

Fig. 8. Potentiostatic current-time curves (plotted logarithmically) recorded on rotating a $(U_{0.95}Gd_{0.05})O_2$ electrode (16.67 Hz) for 1 h in Ar-purged 0.1 M NaCl with 0.05 M $NaHCO_3$/Na_2CO_3, pH = 10.

Fig. 9. Steady-state current density of $(U_{1-y}Gd_y)O_2$ specimens determined potentiostatically at different potentials for 1 hour in 0.1 M NaCl containing 0.05 M Na_2CO_3/NaHCO_3.

Fig. 10. Total anodic charge obtained by integration of the current measured potentiostatically for 1 hour on $(U_{1-y}Gd_y)O_2$ electrodes at different potentials in 0.1 M NaCl containing 0.05 M Na_2CO_3/NaHCO_3.

the doping level (0.2 V) or increases slightly (at 0.3 V to 0.5 V). For $y \geq 0.05$, the current decreases with further increases in Gd content. Perhaps a more reliable measure of the influence of Gd-doping can be obtained by integrating the potentiostatic currents measured over the full 60 minute period. The total anodic charges obtained in this manner are shown in Fig. 10. For anodic oxidation at a potential in region 1 (0.1 V), there is no observable influence of Gd content on the charge accumulated. This confirms that the formation of the thin $U_{1-2x}^{IV}U_{2x}^{V}O_{2+x}$ is not measurably influenced by Gd-doping. At a slightly higher applied potential (0.2 V), when dissolution as $U^{VI}O_2(CO_3)_2^{2-}$ is occurring, the trends observed for steady-state currents are confirmed, the charge either remaining constant or increasing slightly over the doping range $0.01 \leq y \leq 0.05$ and then decreasing with y at higher doping levels ($y > 0.05$).

These effects can be interpreted based on the XRD and Raman spectroscopic observations. The XRD data shows that an increase in doping level leads to a contraction of the UO_2 lattice. This would be expected to inhibit the incorporation of O^{II} ions into interstitial sites (O_I) and their transport to sub-surface locations in the UO_2 fluorite lattice, which should inhibit the oxidation process. By contrast, the increase in Gd^{III} content should also lead to an increase in the number of O_v, which

should increase the rate of oxidation by providing additional sites for the inclusion of O_I.

The changes in current and charge with Gd content suggest a competition between these two effects. The slight increase in current and charge could be taken to indicate a slight increase in anodic reactivity (for the second stage of oxidation) at low doping levels, while the clear decrease in reactivity at higher doping levels could reflect the lattice contraction which is marked at the highest levels. It is also possible that the clear decrease at higher doping levels, while only small, demonstrates the formation of Gd^{III}-O_v clusters, as indicated by the changes in the Raman spectra with doping, a process that would also retard oxidation by decreasing the availability of the O_v required to accommodate additional O_I.

4. Conclusions

A series of $(U_{1-y}Gd_y)O_2$ materials (y = 0, 0.01, 0.03, 0.05, 0.07 and 0.10) were characterized by XRD and Raman spectroscopy to study the influence of Gd^{III} doping on the structure of $(U_{1-y}Gd_y)O_2$ solid solutions. XRD shows that the materials retain a fluorite lattice, which contracts as the Gd content increases up to 10%. Raman spectroscopy shows that Gd^{III} doping distorts the fluorite lattice structure, leading to the formation of oxygen vacancies (O_v)

and, possibly, MO_8-type complexes, since both the oxidation state and ionic radius of Gd^{3+} differ from those of U^{4+}.

The reactivity of the $(U_{1-y}Gd_y)O_2$ specimens were compared electrochemically. Oxidation of $(U_{1-y}Gd_y)O_2$ proceeded in two stages: (1) the oxidation of a thin surface layer to a mixed U^{IV}/U^{V} oxide $(U^{IV}_{1-2x}U^{V}_{2x}O_{2+x})$; (2) the oxidation of this $U^{IV}_{1-2x}U^{V}_{2x}O_{2+x}$ layer to U^{VI}, which dissolved as $U^{VI}O_2(CO_3)^{2-}_2$ in the carbonate-containing solution.

No influence of Gd content was observed on the first stage of oxidation. For the second stage, the anodic reactivity appeared to increase very slightly up to $y = 0.05$, possibly due to the formation of (O_v)s. At higher doping levels, a clear decrease in reactivity was observed which could reflect the lattice contraction which becomes marked at these doping levels.

Overall the increase in doping does not exert a major influence on reactivity, possibly due to this competition between an increase in the number of O_v and a contraction in the lattice constant.

Acknowledgement

References

[1] Choosing a way forward: The future management of Canada's used nuclear fuel, Nuclear Waste Management Organization, Toronto, 2005. http://www.nwmo.ca.

[2] Implementing adaptive phased management 2016 to 2020, Nuclear Waste Management Organization, Toronto, 2016. http://www.nwmo.ca.

[3] J. McMurry, D. Dixon, J. Garroni, B. Ikeda, S. Stroes-Gascoyne, P. Baumgartner, T. Melnyk, Evolution of a Canadian deep geologic repository: base scenario, Report 06819-REP-01200-10092-R00, Ontario Power Generation, Toronto, 2003.

[4] D. Shoesmith, F. King, B. Ikeda, An assessment of the feasibility of indefinite containment of Canadian nuclear fuel wastes, Report AECL-10972 COG-94-534, Whiteshell Laboratories, Atomic Energy of Canada Limited, Pinawa, 1995.

[5] F. King, M. Kolar, The copper container corrosion model used in AECL's second case study, Report 06819-REP-01200-10041-R00, Ontario Power Generation, Toronto, 2000.

[6] D. Shoesmith, Fuel corrosion processes under waste disposal conditions, J. Nucl. Mater. 282 (2000) 1.

[7] M. Trummer, O. Roth, M. Jonsson, H_2 inhibition of radiation induced dissolution of spent nuclear fuel, J. Nucl. Mater. 383 (2009) 226.

[8] E. Ekeroth, O. Roth, M. Jonsson, The relative impact of radiolysis products in radiation induced oxidative dissolution of UO_2, J. Nucl. Mater. 355 (2006) 38.

[9] H. He, M. Broczkowski, K. O'Neil, D. Ofori, O. Semenikhin, D. Shoesmith, Corrosion of nuclear fuel (UO_2) inside a failed nuclear waste container, Report NWMO TR-2012-09, Nuclear Waste Management Organization, Toronto, ON, 2012.

[10] R. McEachern, P. Taylor, A review of the oxidation of uranium dioxide at temperatures below 400 °C, J. Nucl. Mater. 254 (1998) 87.

[11] L. Thomas, R. Einziger, H. Buchanan, Effect of fission products on air-oxidation of LWR spent fuel, J. Nucl. Mater. 201 (1993) 310.

[12] J. Choi, R. McEachern, P. Taylor, D. Wood, The effect of fission products on the rate of U_3O_8 formation in SIMFUEL oxidized in air at 250 °C, J. Nucl. Mater. 230 (1996) 250.

[13] Z. Talip, T. Wiss, P. Raison, J. Paillier, D. Manara, J. Somers, R. Konings, Raman and X-ray studies of uranium-lanthanum-mixed oxides before and after air oxidation, J. Am. Ceram. Soc. 98 (2015) 2278.

[14] G. You, K. Kim, D. Min, S. Ro, Oxidation kinetic changes of UO_2 by additive addition and irradiation, J. Nucl. Mater. 277 (2000) 325.

[15] J. Kim, Y. Ha, S. Park, K. Jee, W. Kim, Effect of a trivalent dopant, Gd^{3+}, on the oxidation of uranium dioxide, J. Nucl. Mater. (2001) 327.

[16] M. Razdan, D. Shoesmith, The electrochemical reactivity of 6.0 wt% Gd-doped UO_2 in aqueous carbonate/bicarbonate solutions, J. Electrochem. Soc. 161 (2014) H225.

[17] M. Razdan, D. Shoesmith, Influence of trivalent-dopants on the structural and electrochemical properties of uranium dioxide (UO_2), J. Electrochem. Soc. 161 (2014) H105.

[18] P. Boczar, J. Griffiths, I. Hastings, Extended burnup in CANDU, Proceedings of an Advisory Group Meeting, Impact of extended burnup on the nuclear fuel cycle, Vienna, 2-5 December, 1991, IAEA Austria, 1993 p. 23.

[19] K. Iwasaki, T. Matsui, K. Yanai, R. Yuda, Y. Arita, T. Nagasaki, N. Yokoyama, I. Tokura, K. Une, K. Harada, Effect of Gd_2O_3 dispersion on the thermal conductivity of UO_2, J. Nucl. Sci. Technol. 46 (2009) 673.

[20] T. Ohmichi, S. Fukushima, A. Maeda, H. Watanabe, On the relation between lattice parameter and O/M ratio for uradium dioxide-trivalent rare earth oxide solid solution, J. Nucl. Mater. 102 (1981) 40.

[21] A. Baena, T. Cardinaels, K. Govers, J. Pakarinen, K. Binnemans, M. Verwerft, Lattice contraction and lattice deformation of UO_2 and ThO_2 doped with Gd_2O_3, J. Nucl. Mater. 467 (2015) 135.

[22] H. He, P. Keech, M. Broczkowski, J. Noël, D. Shoesmith, Characterization of the influence of fission product doping on the anodic reactivity of uranium dioxide, Can. J. Chem. 85 (2007) 702.

[23] H. He, D. Shoesmith, Raman spectroscopic studies of defect structures and phase transition in hyper-stoichiometric UO_{2+x}, Phys. Chem. Chem. Phy. 12 (2010) 8108.

[24] L. Desgranges, G. Baldinozzi, P. Simon, G. Guimbretière, A. Canizares, Raman spectrum of U_4O_9: a new interpretation of damage lines in UO_2, J. Raman Spectrosc. 43 (2012) 455.

[25] D. Manara, B. Renker, Raman spectra of stoichiometric and hyperstoichiometric uranium dioxide, J. Nucl. Mater. 321 (2003) 233.

[26] G. Guimbretière, A. Canizarès, L. Desgranges, R. Caraballo, F. Duval, C. Jegou, M. Magnin, P. Simon, In situ Raman estimation of irradiation-induced heating of UO_2, J. Nucl. Mater. 478 (2016) 172.

[27] L. Li, F. Chen, J. Lu, M. Luo, Study of defect sites in $Ce_{1-x}M_xO_{2-\delta}$ (x = 0.2) solid solutions using Raman spectroscopy, J. Phys. Chem. A 115 (2011) 7972.

[28] K. Park, D. Olander, Defect models for the oxygen potentials of gadolinium and europium-doped urania, J. Nucl. Mater. 187 (1992) 89.

[29] L. Desgranges, Y. Pontillon, P. Matheron, M. Marcet, P. Simon, G. Guimbretière, F. Porcher, Miscibility gap in the U–Nd–O phase diagram: a new approach of nuclear oxides in the environment? Inorg. Chem 51 (2012) 9147.

[30] D. Shoesmith, S. Sunder, W. Hocking, Electrochemistry of UO_2 nuclear fuel, in: J. Lipkowski, P. Ross (Eds.), Electrochemistry of Novel Materials, Ch. 6, VCH publishers, New York, 1994 p. 297.

[31] T. Kubo, S. Ishimoto, T. Koyama, Effects of gadolinium doping on electrical properties of UO_2 grain boundaries, J. Nucl. Sci. Technol. 30 (1993) 664.

[32] Z. Liu, S. Gao, J. Ouyang, X. Xia, Influence of MoO_3 doping on structure and electrical conductivity of defect fluorite-type $Gd_2Zr_2O_7$, J. Alloys Compd. 506 (2010) 868.

[33] T. Van Dijk, K. De Vries, A. Burggraaf, Electrical conductivity of fluorite and pyrochlore $Ln_xZr_{1-x}O_{(1-x)/2}$ (Ln = Gd, Nd) solid solutions, Phys. Stat. Sol. (a) 58 (1980) 115.

[34] J. Faber, C. Geoffroy, A. Roux, A. Sylvestre, P. Abelard, A systematic investigation of the dc electrical conductivity of rare-earth doped ceria, Appl. Phys. A 49 (1989) 225.

[35] B. Santos, J. Noël, D. Shoesmith, The effect of pH on the anodic dissolution of SIMFUEL (UO_2), J. Electroanal. Chem. 586 (2006) 1.